On the statistical behavior of homogenized properties and ultrasonic phase velocities in random polycrystals

Ningyue Sheng, Shahram Khazaie, Mathilde Chevreuil, Sylvain Fréour

On the statistical behavior of homogenized properties and ultrasonic phase velocities in random polycrystals

Ningyue Sheng[a], Shahram Khazaie[a,*], Mathilde Chevreuil[a], Sylvain Fréour[a]

[a] *Nantes Université, Ecole Centrale Nantes, CNRS, GeM, UMR 6183, F-44000 Nantes, France*

Abstract

Most theoretical studies on homogenized properties of polycrystals consider infinite textureless media with orientations characterized by independent Euler angles. However, microstructural analyses of polycrystals reveal spatially correlated orientations of grains whose sizes often follow lognormal distributions. Moreover, experimental investigations show that the single-crystal elastic constants (SEC) in the crystallite's local coordinates could exhibit variabilities. To the best of our knowledge, in the context of our study, these have never been considered in the literature. In this paper, the crystal orientations are simulated using random fields (RFs) with different correlation parameters. A maximum entropy principle is used to simulate realizations of the local stiffness matrices. Numerical results indicate that generating Euler angles using independent random variables is legitimate when correlation lengths of orientations are close enough to the average grain size. Analytical formulas are derived to estimate the statistical behavior of effective elastic moduli and the phase velocities considering either unimodal or bimodal grain

*shahram.khazaie@univ-nantes.fr

[1] https://doi.org/10.1016/j.ijsolstr.2023.112531

size distributions and fluctuations in local tensors for both two- and three-dimensional polycrystals. The former highlight the important roles of the coefficient of variations of the grain sizes and that of the elastic constants. This work contributes to microstructural characterization research associated with ultrasonic phase velocity measurements.
Keywords: Random polycrystals, Homogenization, Random fields, Phase velocities, Grain size distribution

1. Introduction

Metals and their alloys are polycrystalline materials that are widely used in industry. Polycrystals consist of discrete grains or crystallites whose macroscopic properties are often of great importance. The latter depend on the SEC, the morphological characteristics, and the crystallographic orientations of the grains. Over recent decades, numerous theoretical investigations have been conducted to determine the effective elastic modulus of polycrystalline materials in infinitely large polycrystals having equally sized grains with no preferred, spatially uncorrelated crystallographic orientations [1–3]. As such, the overall elastic modulus is isotropic and deterministic. Nonetheless, in practice, polycrystalline samples have a finite number of crystals, resulting in a non-vanishing degree of anisotropy, which can be detected using non-destructive evaluation (NDE) techniques, e.g., ultrasonic wave measurements [4, 5]. Consequently, the effective elastic properties exhibit variations between different samples as reported in theoretical and numerical studies [6–11]. Experimental works also revealed the influence of medium size and number of grains on the mechanical properties such as effective stress and tensile

strength [12–14].

Moreover, the single-crystal elasticity matrix in the crystallite's local reference frame is considered deterministic in the literature. However, several studies on the elastic moduli of alpha iron (α-Fe) monocrystals report different values. Table A.1 in Appendix A provides the values summarized by Cantara *et al.* [15], along with the corresponding first- and second-order statistics. For this particular case, it turns out that the component c_{12} has the largest coefficient of variation (CV), i.e., 6%. Thus, it becomes imperative to validate the prevalent assumption of deterministic local stiffness tensors and investigate the impact of introducing fluctuations in these tensors on the effective elastic properties and their statistical properties. Besides, for simplicity purposes, the crystallographic orientations, represented by a triplet of Euler angles $(\Theta_1, \Theta, \Theta_2)$, are often considered independent random variables with particular marginal probability density functions (PDFs) resulting in uniformly distributed rotations provoking a faster convergence to an isotropic background [16]. However, many microstructural investigations on polycrystals using the electron backscatter diffraction (EBSD) technique have revealed that the neighboring grains can exhibit statistically closer orientations, implying their inherent spatial correlations [17–21]. This phenomenon can be attributed to various factors, including the manufacturing techniques like rolling, which can induce the morphological texture and subsequently contribute to the spatial correlation of the Euler angles [17, 18, 20]. Additionally, the spatial correlation could also stem from the grain growth processes, such as the presence of twinning relationships observed in alloy 304 stainless steel [21]. Furthermore, experimental studies have reported the

existence of large regions comprising equiaxed primary grains with similar crystallographic orientations [22]. These regions, referred to as macrozones, exhibit relatively long correlation lengths (up to 100 times the average grain size) of the orientations [22]. Several numerical studies concerning simulating these spatially correlated orientations have been carried out [19, 23–25]. Here, a random field-based generation of the Euler angles is to be incorporated into our numerical model. Consequently, the influence of the spatially correlated orientations on the statistical properties of homogenized elastic modulus tensor needs to be investigated. Note that our study is centered on synthetic polycrystals featuring equiaxed grains without morphological texture. Furthermore, polycrystals composed of equiaxed grains commonly exhibit lognormal grain size distributions [14, 26]. The distribution width has a major effect on the mechanical properties, e.g., the tensile stress [27], the yield stress [28], and the flow stress [29, 30]. Recently, there has been considerable interest in bimodal grain size distributions in polycrystals. By employing techniques such as powder metallurgy and spark plasma sintering, precise control over the grain size distributions and the volume fractions can be achieved [31, 32]. These bimodal grain size distributions could be highly influential on the mechanical properties such as the strength and ductility [31, 32], along with the chemical properties such as the corrosion behavior [33]. The effect of unimodal and bimodal grain size distributions on ultrasonic wave propagation in polycrystals has been widely studied [34–36], showing promise in measuring ultrasonic scattering-induced attenuation to characterize the width of grain size distributions in polycrystalline samples. Other NDE applications based on phase velocity measurements include

the estimation of average grain size [37], characterizing temperature-related changes and levels of cold working [38], assessing annealing behavior, and quantifying recrystallization levels [39]. However, most previous studies predominantly focused on the mean response (first-order statistics) of variables of interest (VoI). Therefore, it is essential to investigate and quantify the influence of the grain size distribution on the second-order statistics of effective elastic properties and, consequently, on those of ultrasonic phase velocities.

In this work, the open-source software NEPER [40] is used to generate multiple realizations of synthetic polycrystals with unimodal and bimodal grain size distributions with different widths. The crystallographic orientations of grains are simulated as spatially correlated RFs with different correlation parameters. Besides, following Guilleminot and Soize [41], the uncertainty on the SEC is taken into account via a maximum entropy principle. Our investigation focuses on the influence of the aforementioned parameters, including correlated orientations, grain size distributions, and single-crystal elastic moduli fluctuations, on the statistical behavior of the homogenized elastic moduli and the phase velocities. Explicit formulas for second-order statistics of effective elastic moduli and phase velocities expressed in terms of the width of the grain size distribution, number of grains, and elastic properties of the material are derived and validated via numerical simulations.

This paper is organized as follows: Sec. 2 presents the numerical model construction, including the RF-based generation of crystallographic orientations and random single-crystal elasticity tensors, as well as the computational framework of the effective elastic properties and the phase velocities in polycrystalline materials. Analytical and numerical results are shown in

Sec. 3, with a discussion about the statistical characteristics of the effective elastic moduli and the ultrasonic phase velocities concerning various input random parameters.

2. Numerical model construction and computational framework

2.1. Generation of synthetic polycrystals

A large number of synthetic cubic polycrystals defined by $\Omega = \{\boldsymbol{x} = (x, y, z) \in \mathbb{R}^3 \,|\, 0 \leq x, y, z \leq 1000\,\mu\text{m}\}$, composed of equiaxed grains have been generated via the open-source software NEPER [42] to study the statistical properties of our VoI, i.e., the effective elastic moduli, and the phase velocities. It is worth mentioning that NEPER uses the so-called Laguerre (weighted Voronoï) tessellation and can create microstructures that are consistent with experimental observations, for which the grain equivalent diameters follow a lognormal distribution [42], as frequently reported in the literature [14, 26]. Table 1 summarizes the samples generated via this approach, named **PSD26-i**, $i \in \{1, 2, ..., 8\}$, wherein the number of grains N_g varies from 500 to 30000 and 26 means that the CV of the grain size distribution is about 26%. Since the lognormal distribution is often used to model the equivalent diameter random variable D [14, 28, 29], the former will be used in this work. As such, $D \sim \text{Lognormal}\big(\bar{D}, \sigma_D\big)$, where $\bar{D}$, σ_D are the mean and standard deviation of D, respectively. The latter, along with the corresponding CV, denoted by δ_D, for each set, are reported in Table 1. Note that the values of δ_D for these samples are relatively small compared to some real samples, such as recrystallized aluminum (Al) polycrystals, where it may even exceed 1 [26]. By reshuffling the seeds of the underlying distribu-

tion, which implies changing the grains' centroid locations, 200 realizations have been generated for each set. Fig. 1(a) shows one realization of the set **PSD26-4**, where grains are distinguished by different colors. The PDF of the grain equivalent diameters and that of the grain volumes are depicted in Figs. 1(b) and (c), respectively.

Table 1: Polycrystal samples and the corresponding statistical properties of D.

Set	N_g	$\bar{D}$ [μm]	σ_D [μm]	δ_D [-]
PSD26-1	500	146.8	37.8	0.257
PSD26-2	1000	116.5	29.9	0.257
PSD26-3	5000	68.2	17.4	0.256
PSD26-4	10000	54.1	13.8	0.255
PSD26-5	15000	47.3	12.1	0.255
PSD26-6	20000	42.9	11.0	0.255
PSD26-7	25000	39.9	10.2	0.255
PSD26-8	30000	37.5	9.6	0.255

2.2. Simulation of crystallographic orientations

This section aims to simulate the crystallographic orientations of the grains constituting the polycrystalline samples, characterized by a random vector of Euler angles $(\Theta_1, \Theta, \Theta_2)$ described hereinafter by the RFs (Y_1, Y_2, Y_3). Two cases of uncorrelated and correlated Euler angles are to be distinguished. The former is based on generating them via $(2\pi X_1, \arccos(-1 + 2X_2), 2\pi X_3)$ where $X_i \sim \mathrm{U}[0, 1]$, $i \in \{1, 2, 3\}$, are independent uniform random variables [16]. Such distributions of the Euler angles provoke faster convergence

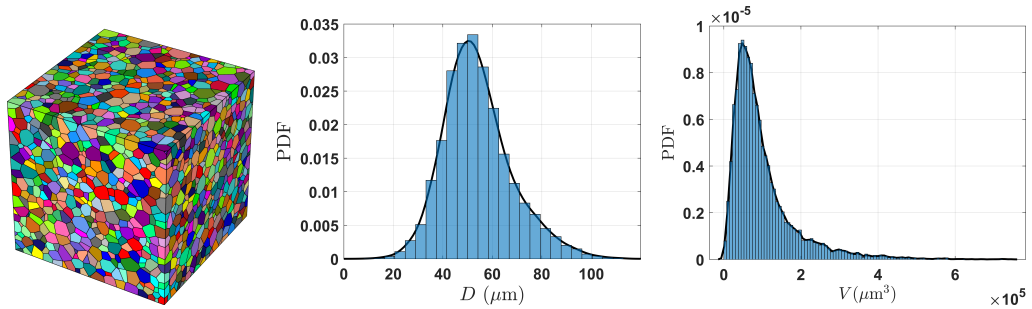

(a) (b) (c)

Figure 1: (Color online) (a) A realization of the set **PSD26-4**, (b) the PDF of equivalent diameters D, and (c) the PDF of grain volumes V.

towards the statistical isotropy. On the other hand, the simulation of the spatially correlated orientations is based on the construction of non-Gaussian RFs. For this purpose, independent Gaussian RFs $Z_i(\boldsymbol{x})$, $i \in \{1,2,3\}$, are first generated using the Karhunen-Loève expansion (KLE) [43]. The truncated series expansion of these RFs read:

$$Z_i(\boldsymbol{x}) \approx \sum_{j=1}^{N_g} \sqrt{\lambda_j^i}\omega_j^i\psi_j^i(\boldsymbol{x}), \tag{1}$$

where $\boldsymbol{x} \in \boldsymbol{\Omega}$ and $\left\{\lambda_j^i, \psi_j^i\right\}$ are the eigenvalues with their corresponding eigenfunctions of the target autocovariance function (ACF) of the RF Y_i, $i \in \{1,2,3\}$, denoted by $R_{Y_iY_i}$. The ACFs are assumed to depend on the distance between two points, i.e., $R_{Y_iY_i}(\boldsymbol{x_m}, \boldsymbol{x_n}; l_{Y_i}) = \sigma_{Y_i}^2 \hat{R}_{Y_iY_i}(\xi = \|\boldsymbol{x_m} - \boldsymbol{x_n}\|/l_{Y_i})$, where $(\boldsymbol{x_m}, \boldsymbol{x_n}) \in \boldsymbol{\Omega} \times \boldsymbol{\Omega}$ and l_{Y_i} is the correlation distance or the typical size of the heterogeneities. In Eq. (1), ω_j^i, $i \in \{1,2,3\}$, is a vector of j independent standard Gaussian random variables. The corresponding non-Gaussian RF then writes $Y_i(\boldsymbol{x}) = F_{Y_i}^{-1}(\boldsymbol{\Phi}(Z_i(\boldsymbol{x})))$, where $F_{Y_i}(a) = \int_{-\infty}^{a} p_{Y_i}(t)\mathrm{d}t$ is the

cumulative distribution function (CDF) of Y_i with target PDF p_{Y_i}, and $\mathbf{\Phi}(\cdot)$ is the CDF of the standard Gaussian distribution.

2.3. Simulation of random single-crystal elasticity tensors

For the materials with cubic symmetry, the fourth-order elasticity tensor of a single crystal in the local reference is fully characterized by three independent parameters and can be written as the linear combination $\mathbb{C}^{(\mathrm{cr})} = \lambda_m \mathbb{E}^{(m)}$, where the linearly independent fourth-order basis tensors $\mathbb{E}^{(m)}$, $m \in \{1, 2, 3\}$, are given by Moakher and Norris [44]. Note that the Einstein summation convention is implied whenever each index is repeated twice. Throughout the paper, the superscript (cr) is used to indicate that the corresponding elastic tensor (matrix) is considered in crystallite's local reference, and it corresponds to the global reference frame otherwise. A Voigt representation of $\mathbb{C}^{(\mathrm{cr})}$ as a 6×6 matrix $C^{(\mathrm{cr})}$ will be used for the sequel. This matrix has three positive eigenvalues $(\lambda_1, \lambda_2, \lambda_3) = (c_{11} + 2c_{12}, 2c_{44}, c_{11} - c_{12})$ with the corresponding multiplicity of 1, 3, and 2, respectively. Since in the framework of this study, the only available information about the stiffness matrix is its mean and fluctuation level, along with some physical constraints (positive-definiteness and invertibility), a non-parametric probabilistic model using the random matrix theory in conjunction with the maximum entropy principle will be used to generate realizations of the matrix $C^{(\mathrm{cr})}$ [41, 45]. Following Guilleminot and Soize [41], the random eigenvalues λ_m, $m \in \{1, 2, 3\}$, will be modeled as three independent gamma distributed random variables $\mathrm{G}(k_m, s_m)$, where (k_m, s_m) are the corresponding shape and scale parameters such that $\bar{\lambda}_m = k_m s_m$ and $\sigma^2_{\lambda_m} = k_m s_m^2$. The PDFs of these eigenvalues

write:

$$\lambda_1 \sim \mathrm{G}\left(\frac{1+2\epsilon^2}{3\epsilon^2}, \frac{3\left(\bar{C}_{11}+2\bar{C}_{12}\right)\epsilon^2}{1+2\epsilon^2}\right),$$
$$\lambda_2 \sim \mathrm{G}\left(\frac{1}{\epsilon^2}, 2\bar{C}_{44}\epsilon^2\right), \tag{2}$$
$$\lambda_3 \sim \mathrm{G}\left(\frac{2+\epsilon^2}{3\epsilon^2}, \frac{3\left(\bar{C}_{11}-\bar{C}_{12}\right)\epsilon^2}{2+\epsilon^2}\right),$$

where $\epsilon \in \mathbb{R}^+$ is defined as $\epsilon = \delta_{\lambda_2} = \delta_{C_{44}}$. It is worth noting that ϵ controls the global fluctuation level of the random matrix $C^{(\mathrm{cr})}$. Given the lack of monocrystal elastic modulus data for different materials, we chose a range of values for $\epsilon \in [0, 0.02]$ to account for a variety of plausible fluctuation levels for the polycrystals of our interest. The upper bound has been chosen based on the experimental values for alpha iron (α-Fe, Table A.1 in Appendix A).

2.4. Computational framework for effective elastic moduli

Homogenization techniques are used to calculate the effective properties C^{eff} of polycrystals. Since our main objective is to estimate the variability of C^{eff}, the latter should be calculated on different realizations using analytical methods instead of computationally demanding numerical homogenization techniques, allowing us to estimate C^{eff} faster. To this end, the classical Voigt [1] and Reuss [2] averaging techniques provide upper and lower bounds for C^{eff}. On the other hand, the self-consistent (SC) technique, originally developed by Hershey [46], Eshelby [47], and Kröner [3], involves using the equivalent inclusion method under the small deformation and linear elasticity assumption. This technique considers that the strain of the embedded inclusion ϵ_{kl} is related to the applied uniform far-field macroscopic strain ϵ^*_{kl} on the unbounded homogeneous isotropic background as $\epsilon_{ij} = \mathbb{B}_{ijkl}\epsilon^*_{kl}$, where

$\mathbb{B}_{ijkl}$ is the concentration tensor. The SC technique provides more accurate estimates of C^{eff} compared to the Voigt and Reuss averaging approaches, as confirmed by experimental results [48]. Lubarda [49] extended the SC method by representing the crystallites inside the polycrystals as embedded spherical inclusions with cubic symmetry inside the background. In this case, the SC elastic modulus of the n^{th} crystallite can be expressed as $\mathbb{C}^{\text{sc,n}}_{ijkl} = \mathbb{C}^{(\text{cr})}_{ijmn}\mathbb{B}_{mnkl}$. The effective elasticity tensor of a polycrystal with volume (area) $V = |\Omega|$ based on the SC approach can then be estimated by volume averaging of $\mathbb{C}^{\text{sc,n}}_{ijkl}$, i.e., $\mathbb{C}^{\text{eff,sc}}_{ijkl} = \sum_{n=1}^{N_g} \mathbb{C}^{\text{sc,n}}_{ijkl} V_n/V$, where V_n is the volume (area) of each grain [9, 49]. This SC approach-based effective elasticity tensor could be further decomposed as the sum of isotropic and anisotropic tensors $\mathbb{C}^{\text{eff,sc}}_{ijkl} = \mathbb{C}^{\text{iso,sc}}_{ijkl} + \mathbb{C}^{\text{ani,sc}}_{ijkl}$ where $\mathbb{C}^{\text{iso,sc}}_{ijkl}(h) = [hc_{11} + (1-h)c_{12}]\delta_{ij}\delta_{kl} + 2(1+2h)c_{44}\mathbb{I}_{ijkl}$ and $\mathbb{C}^{\text{ani,sc}}_{ijkl}(h) = \nu_{\text{sc}}(h)\sum_{n=1}^{N_g} \mathbb{A}^{n}_{ijkl} V_n/V$ in which ν_{sc} is the SC anisotropy coefficient defined as $\nu_{\text{sc}}(h) = (c_{11} - c_{12} - 2c_{44})(1-3h) - 10hc_{44}$. In these equations, δ_{ij} is the Kronecker symbol (1 if $i = j$ and 0 otherwise), $\mathbb{I}$ and $\mathbb{A}$ are the fourth-order identity and rotation tensors, and h is a measure of the distance between the concentration tensor $\mathbb{B}$ and the fourth-order identity tensor $\mathbb{I}$. Note that h is a function of the elastic constants (see Eq. (8) in Kube and Turner [50]). Analogous equations hold for the Voigt and Reuss-averaged estimates. In particular, for the Voigt method, it suffices to put $h = 0$ in the SC formulas, i.e., $\mathbb{C}^{\text{eff,v}}_{ijkl} = \mathbb{C}^{\text{iso,v}}_{ijkl} + \mathbb{C}^{\text{ani,v}}_{ijkl}$ where $\mathbb{C}^{\text{iso,v}}_{ijkl} = \mathbb{C}^{\text{iso,sc}}_{ijkl}(h = 0)$ and $\mathbb{C}^{\text{ani,v}}_{ijkl} = \nu_{\text{v}} \sum_{n=1}^{N_g} \mathbb{A}^{n}_{ijkl} V_n/V$ in which $\nu_{\text{v}} = \nu_{\text{sc}}(h = 0) = c_{11} - c_{12} - 2c_{44}$ is the anisotropy coefficient. It is worth mentioning that the Reuss averaging will not be used in this paper since it yields the variabilities of the effective compliance tensor that cannot be simply related to those of the effective

modulus tensor. In Sec. 3.1, the statistical parameters of the components of the tensor $\mathbb{C}^{\text{eff}}_{ijkl}$ will be investigated.

2.5. Computational framework for plane wave phase velocities

The plane P and S wave phase velocities v and their corresponding polarization directions $\mathbf{w}$ can be calculated by solving the following eigenvalue problem known as the Christoffel equation [51]:

$$\left(\mathbb{C}^{\text{eff}}_{mnop}\hat{k}_n\hat{k}_o - \rho v^2\delta_{mp}\right) w_p = 0, \tag{3}$$

in which $\hat{\mathbf{k}}$ is the propagation direction, and ρ is the density of the material considered deterministic constant. Defining the second-order tensor $\Lambda_{mp}(\hat{\mathbf{k}}) = \mathbb{C}^{\text{eff}}_{mnop}\hat{k}_n\hat{k}_o$, Eq. (3) can be written in the matrix form $(\mathbf{\Lambda} - \rho v^2\mathbf{I}_3)\mathbf{w} = \mathbf{0}$ where $\mathbf{I}_3$ denotes the 3×3 identity matrix. The phase velocities and polarization directions are then calculated by looking for the eigenvalues and eigenvectors of the matrix $\mathbf{\Lambda}$.

It is worth noting that the presence of anisotropic behavior is inherent in our finite-sized polycrystals due to their finite volumes. The propagation of ultrasonic waves within an anisotropic medium induces quasi-longitudinal and quasi-shear waves whose polarization directions deviate from the propagation direction $\hat{\mathbf{k}}$ [51]. In Sec. 3.2, the statistics of the P and S wave phase velocities will be investigated.

3. Analytical and numerical results

Different cubic materials are used for our subsequent numerical investigations. Table 2 summarizes their average elastic constants along with their anisotropy levels defined as $\hat{A} = |1 - A_Z| = |\nu_{\text{v}}|/(c_{11} - c_{12})$, where

$A_Z = 2c_{44}/(c_{11} - c_{12})$ is the classical Zener index [52]. These materials have been chosen to cover a range of anisotropy levels. Note that when $\hat{A}$ tends to 0, the material tends to be elastically isotropic. The influence of the correlated Euler angles, the random local stiffness tensor, along with the distribution width of grain sizes on the statistical behavior of different components of the effective elasticity matrix C^{eff} will be investigated in Sec. 3.1. We mainly focus on the dominant components $IJ \in \{11, 12, 66\}$ of C^{eff}. The statistical properties of the phase velocities will be then studied in Sec. 3.2.

Table 2: Average SEC and the corresponding anisotropy levels for different cubic materials [15, 53].

Name	$\bar{C}_{11}$ [GPa]	$\bar{C}_{12}$ [GPa]	$\bar{C}_{44}$ [GPa]	$\hat{A}$ [-]
Al	108	62	28.3	0.23
α-Fe	231	135	115	1.40
Co	242	160	128	2.12
γ-Fe	154	122	77	3.81
Li	13.4	11.3	9.6	8.14

3.1. Influence on the statistical properties of effective elastic moduli

3.1.1. Influence of correlated crystallographic orientations

The investigations in [18, 19] based on EBSD data obtained from real polycrystalline samples revealed exponential kernel functions as the most suitable fitting function type for the ACFs of the Euler angles. An exponential ACF, even though it is the most frequent choice in the literature, has shown its limitations in the description of the microstructure of some polycrystals [54]. Recently, a von Kármán ACF has been suggested to describe

wave propagation in polycrystals [55]. This model covers a range of correlations by varying the so-called Hurst number. In this study, because of the lack of experimental data and following [56, 57], we compared different ACFs summarized in Table 3. Note that extensive numerical investigations have been conducted in our study using other ACF types that are not included in this table. However, it was determined that the statistical properties of the homogenized elastic moduli did not exhibit significant differences when compared to the values presented in Table 3. As such, our subsequent investigations are based only on these models. Besides, as noted by Arwade and Grigoriu [19], long-range correlations in orientations within various aluminum alloy polycrystals have been identified [17]. Moreover, the existence of large regions composed of equiaxed primary grains sharing similar crystallographic orientations as macrozones has been reported [22]. Thus, in order to represent a range for the characteristic length of the heterogeneities, two different cases are considered, where the ratio $t = l_{Y_i}/\bar{D}$ is either 2 or 5. These cases are specified by the superscripts s (short) and l (long), respectively. Note that for simplicity purposes, the correlation lengths are considered the same for different Euler angles, and the cross-correlations are not considered. As a result, the Euler angles are considered independent, whose joint PDF yields equally likely random rotations.

The statistical properties of the effective elastic moduli for 3D synthetic polycrystals composed of different materials listed in Table 2 are investigated via the SC approach. Note that achieving isotropic (non-preferential) orientations for our finite-volume synthetic polycrystals is impossible. As a result, multiple realizations have been generated for each polycrystal sample

Table 3: Definition of different kernel functions [57].

ACF type	$\hat{R}_{YY}(\xi)$
Exponential	$\exp\left(-2\xi\right)$
Low-pass white noise	$\frac{3\left(\sin\left(\frac{3\pi}{2}\xi\right)-\frac{3\pi}{2}\xi\cos\left(\frac{3\pi}{2}\xi\right)\right)}{\left(\frac{3\pi}{2}\xi\right)^3}$
Power-law	$\left(1+\frac{\pi^2\xi^2}{4}\right)^{-2}$

set. This approach ensures that our VoI, i.e., the statistical properties of effective elastic moduli, remains unaffected by the homogenization method employed for polycrystals with finite volumes. For instance, for the case of **PSD26-1** consisting of 500 grains of lithium (Li), which exhibits the highest level of anisotropy at the scale of the single crystal (see Table 2), the first- and second-order statistical properties of the effective elastic modulus C_{11}^{eff} using the SC approach are presented in Fig. 2. This figure clearly illustrates the statistical convergence of this VoI, as the patterns observed in other elastic components and materials.

The PDFs of the component C_{11}^{eff} computed for the polycrystals of the sets **PSD26-1** and **PSD26-8** having uncorrelated and correlated (exponential ACF with $t = 5$) Euler angles are depicted in Fig. 3 for the particular case of aluminum (Al) grains. As expected, regardless of the details of the spatial correlation of the heterogeneities (ACF and correlation length), the variability (width of the PDFs) of C_{IJ}^{eff} is inversely proportional to the number of grains N_g. Similar results could be obtained in 2D.

Following Norouzian and Turner [9] and with the aim of obtaining universal curves, i.e., independent of the material properties, the components of

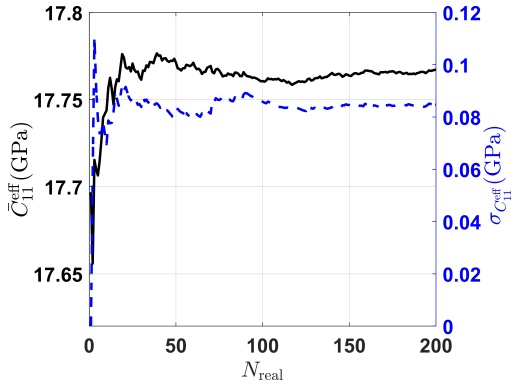

Figure 2: (Color online) Mean $\bar{C}_{11}^{\text{eff}}$ (black solid line) and standard deviation $\sigma_{C_{11}^{\text{eff}}}$ (blue dashed line) of C_{11}^{eff} for lithium (Li) in the sample set **PSD26-1** in terms of the number of samples.

the matrix C^{eff} are normalized by the corresponding anisotropy coefficients ν. We thus define the random variable $\hat{C}_{IJ}^{\text{eff}} = C_{IJ}^{\text{eff}}/\nu$ where ν is ν_{v} (resp. ν_{sc}) for the Voigt (resp. SC) averaging techniques. The standard deviations of $\hat{C}_{11}^{\text{eff}}$, estimated via the SC approach for different materials having deterministic local stiffness matrix ($\epsilon = 0$) with different correlation structures, are displayed in a log scale in Fig. 4. Based on this figure, regardless of the details of the correlation function, $\sigma_{\hat{C}_{11}^{\text{eff}}}$ is a linearly decreasing function of N_g on a log scale. Moreover, Fig. 4 reveals that the classical case [9], where the Euler angles are uncorrelated, always leads to lower values of $\sigma_{\hat{C}_{11}^{\text{eff}}}$ compared to the correlated cases. As expected, the difference between the values of $\sigma_{\hat{C}_{11}^{\text{eff}}}$ for uncorrelated and relatively short-range correlated Euler angles ($t = 2$) is negligible. This observation indicates that generating Euler angles using independent random variables (RF_{unc}) is legitimate for the specific cases where they exhibit relatively short correlation lengths compared to the average grain size. This allows for a drastic reduction in the simulation time

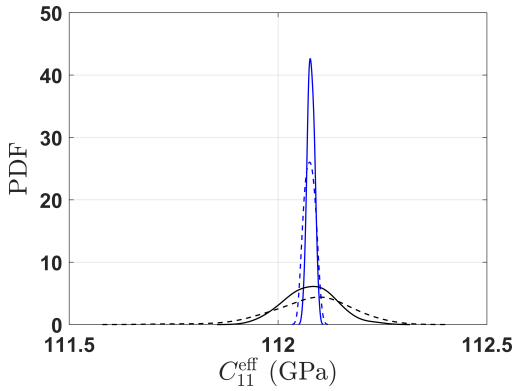

Figure 3: (Color online) PDFs of C_{11}^{eff} for aluminum (Al) in sample sets **PSD26-1** (black), and **PSD26-8** (blue) with uncorrelated (dashed lines), and exponentially correlated Euler angles with $t = 5$ (solid lines).

of the crystallographic orientations. Conversely, increasing the characteristic size of heterogeneity in Euler angles results in a marked increase in $\sigma_{\hat{C}_{11}^{\text{eff}}}$ regardless of the ACF type. Specifically, for $N_g = 500$ and $N_g = 30000$, discrepancies of 39.8% to 73.2% and 44.5% to 215.2% are observed, respectively. This occurs since certain grains aggregate into clusters with close values of Euler angles as the correlation length increases (see Fig. 5, for one realization of the sample set **PSD26-4**). These clusters can be imagined as behaving like "effective grains" with larger effective grain sizes. Consequently, the number of effective grains N_g^{eff} in the polycrystal with a given size becomes smaller compared to the case when Euler angles are uncorrelated. This leads to increased variability in the components of C^{eff}, since the variability is inversely proportional to the number of grains N_g.

Similar linear decreases are observed for the components C_{12}^{eff} and C_{66}^{eff}. A power-type relationship between $\sigma_{\hat{C}_{IJ}^{\text{eff}}}$ and the number of the grains N_g is

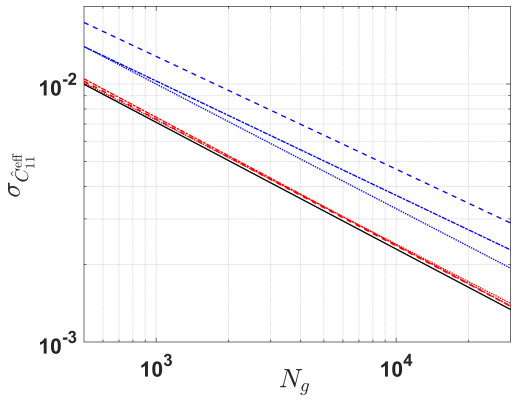

Figure 4: (Color online) $\sigma_{\hat{C}_{11}^{\text{eff}}}$ in terms of N_g for uncorrelated Euler angles RF_{unc} (black solid line), compared with the cases where the Euler angles have relatively short (resp. large) correlation distances $\text{RF}^{\text{s}}_{\text{exp}}$, $\text{RF}^{\text{s}}_{\text{pl}}$ and $\text{RF}^{\text{s}}_{\text{lpw}}$ (resp. $\text{RF}^{\text{l}}_{\text{exp}}$, $\text{RF}^{\text{l}}_{\text{pl}}$ and $\text{RF}^{\text{l}}_{\text{lpw}}$) in dotted, dash-dotted and dashed blue lines (resp. red lines), respectively.

thus proposed (see Norouzian and Turner [9] for details):

$$\sigma_{\hat{C}_{IJ}^{\text{eff}}} = \alpha_{IJ} N_g^{\beta_{IJ}}, \quad IJ \in \{11, 12, 66\}, \tag{4}$$

wherein the coefficients $(\alpha_{IJ}, \beta_{IJ})$ depend on the parameters of the correlation structure and the dimension of the problem d. In this section, we only consider 3D polycrystals, and we analytically extend the results to 2D cases in the next section. The estimated values of the coefficients α_{11} and β_{11} for different case studies are summarized in Table 4. Based on these values, it can be inferred that the value of the index β_{11} increases as the characteristic size of the heterogeneity of Euler angles grows. This trend persists independent of the kernel function used as the ACF of the Euler angles RFs. For the reference case, RF_{unc}, we obtain $(\alpha_{11}, \beta_{11}) = (0.222, 0.497)$ as opposed to $(\alpha_{11}, \beta_{11}) = (0.191, 0.5)$ reported in Norouzian and Turner's work [9]. The discrepancies are $(13.9\%, 0.6\%)$. Besides, Böhlke *et al.* [8]

studied the standard deviation of the Young's modulus of polycrystalline microspecimens and report β_{11} as 0.438 and 0.470, obtained via numerical and analytical approaches, respectively. Compared to our results ($\beta_{11} = 0.497$), the discrepancies are 11.9% and 5.4%. It is worth mentioning that Bohlke *et al.* [8] used models where $N_g \leq 1000$. As such, the insufficient number of grains could lead to an inaccurate estimation of $(\alpha_{11}, \beta_{11})$. The difference could be related to different tessellation types used to generate the microstructures (Voronoï tessellation in our study and voxel-based tessellation in Norouzian and Turner's work [9]) and different grain size statistics ($\delta_D = 0.1$ in Norouzian and Turner [9] as opposed to $\delta_D = 0.255$ in this work). As will be investigated analytically in the next subsection, the width of the grain size distribution is shown to be influential on the values of α_{IJ}.

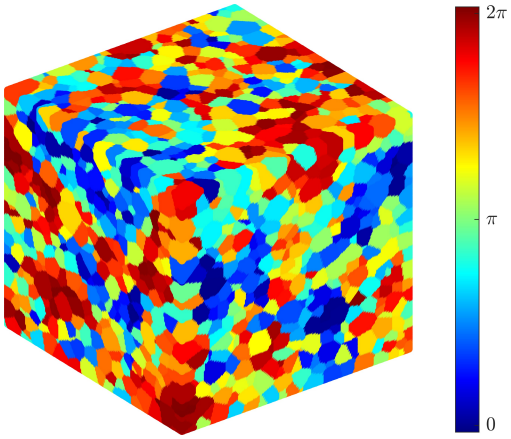

Figure 5: (Color online) Exponentially correlated Euler angle θ_1 with $t = 5$ in one realization of random polycrystals **PSD26-4**.

Table 4: Coefficients α_{11} and β_{11} in Eq. (4) for different numerical case studies.

Case	$\boldsymbol{\alpha_{11}}$	$\boldsymbol{\beta_{11}}$
$\mathbf{RF_{unc}}$	0.222	-0.497
$\mathbf{RF^{s}_{exp}}$	0.201	-0.483
$\mathbf{RF^{l}_{exp}}$	0.281	-0.481
$\mathbf{RF^{s}_{lpw}}$	0.217	-0.491
$\mathbf{RF^{l}_{lpw}}$	0.262	-0.437
$\mathbf{RF^{s}_{pl}}$	0.227	-0.495
$\mathbf{RF^{l}_{pl}}$	0.219	-0.443

3.1.2. Influence of the grain size distribution

In this section, we derive the analytical formulas to estimate $\sigma_{\hat{C}^{\text{eff}}_{IJ}}$ in terms of N_g and δ_D for both 2D and 3D cases. We consider a 3D (resp. 2D) polycrystal composed of N_g grains having random volumes (resp. areas) and orientations. Fig. 6 shows this construction schematically in 2D. Note that the total volume (area) of this sample is also a random variable. As already mentioned, each component of the matrix C^{eff} can be decomposed as the sum of isotropic and anisotropic contributions:

$$\hat{C}^{\text{eff}}_{IJ} = \hat{C}^{\text{eff,iso}}_{IJ}(h) + \frac{\sum_{m=1}^{N_g} f_{IJ_m}(\Theta_1, \Theta, \Theta_2) V_m}{\sum_{m=1}^{N_g} V_m}, \tag{5}$$

wherein V_m (measure of the domain occupied by the grain number m) and f_{IJ_m}, $m \in \{1, \dots N_g\}$, are N_g *iid* random variables. They are realizations of the random variables $V = \pi^{d/2} D^d / (2^d \Gamma(1+d/2))$ and $f_{IJ} = \left[\sum_{n=1}^{3} A_{in} A_{jn} A_{kn} A_{ln}\right]^{kl \to J}_{ij \to I}$, respectively. In these equations, $d \in \{2, 3\}$ is the dimension of the polycrys-

tal, Γ is the gamma function, A is the 3×3 rotation matrix associated with the fourth-order rotation tensor $\mathbb{A}$, and the mapping $ij \to I$ (same for $kl \to J$) is defined as $11 \to 1$, $22 \to 2$, $33 \to 3$, $23 \to 4$, $13 \to 5$, and $12 \to 6$. In Eq. (5), if $h \neq 0$, an SC homogenization method is implied, and the normalization constant is thus $\nu_{\text{sc}}(h)$. However, for the Voigt averaging, one needs to put $h = 0$, which implies a normalization by $\nu_{\text{v}} = \nu_{\text{sc}}(0)$.

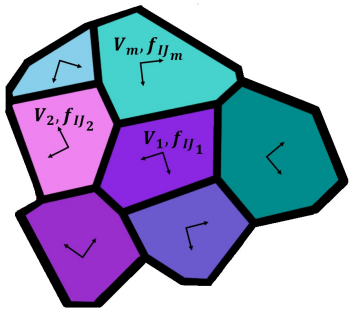

Figure 6: (Color online) Polycrystalline sample with N_g random grains.

First, we suppose that the local elastic moduli C_{IJ} are perfectly known and are thus homogeneous deterministic constants in the medium. The variability of C_{IJ}^{eff} will be solely related to that of the Euler angles (components of the rotation matrix A) and of the grain volumes (areas). In 2D, only one random Euler angle exists and is distributed as $\Theta_1 \sim \text{U}[0, 2\pi]$. Besides, when $d = 3$, since the Euler angles are independent, their joint PDF reads:

$$p_{(\Theta_1,\Theta,\Theta_2)}(\theta_1, \theta, \theta_2) = \frac{\sin(\theta)}{8\pi^2} \mathbb{1}_{[0,2\pi]}(\theta_1) \mathbb{1}_{[0,\pi]}(\theta) \mathbb{1}_{[0,2\pi]}(\theta_2), \tag{6}$$

where $\mathbb{1}_{\mathcal{D}}(x)$ denotes the indicator function that is equal to 1 if $x \in \mathcal{D}$ and 0 otherwise. Therefore, the ensemble (statistical) average of any function of

the Euler angles, say the random variable $\mathcal{F}(\Theta_1, \Theta, \Theta_2)$, writes:

$$\bar{\mathcal{F}} = \frac{1}{8\pi^2} \int_0^{2\pi} \int_0^{\pi} \int_0^{2\pi} \mathcal{F}(\theta_1, \theta, \theta_2) \sin(\theta) \mathrm{d}\theta_1 \mathrm{d}\theta \mathrm{d}\theta_2. \tag{7}$$

Similarly, the variance of f_{IJ} is defined as $\mathrm{Var}(f_{IJ}) = \overline{f_{IJ}^2} - \overline{f_{IJ}}^2$. One can simply show that when $d = 3$, the mean and variances of f_{11}, f_{12} and f_{66} are respectively $(\frac{3}{5}, \frac{16}{525})$, $(\frac{1}{5}, \frac{3}{175})$, and $(\frac{1}{5}, \frac{3}{175})$. On the other hand, these values are $(\frac{3}{4}, \frac{1}{32})$, $(\frac{1}{4}, \frac{1}{32})$, and $(\frac{1}{4}, \frac{1}{32})$ for the 2D case. For the 3D case, as the random variables f_{12} and f_{66} have the same first and second-order statistics, hereinafter, IJ is limited to 11 or 12. However, no difference will be made between indices in 2D. Since the grain equivalent diameters and the Euler angles are considered independent, the ensemble average and the variance of the random variables $f_{IJ_m} V_m$ are $\overline{f_{IJ}}\,\overline{V}$ and $\mathrm{Var}[f_{IJ}]\mathrm{Var}[V] + \mathrm{Var}[f_{IJ}]\overline{V}^2 + \overline{f_{IJ}}^2\mathrm{Var}[V]$, respectively. Since the random variables V_m (resp. $f_{IJ_m} V_m$) are *iid*, the variances of their sum are the sum of each individual variance. We also note that if X and Y are two random variables, a first-order Taylor expansion-based approximation for the variance of the random variable $Z = \frac{X}{Y}$ writes:

$$\mathrm{Var}(Z) \approx \left(\frac{\bar{X}}{\bar{Y}}\right)^2 \left(\delta_X^2 - 2\frac{\mathrm{Cov}(X, Y)}{\bar{X}\,\bar{Y}} + \delta_Y^2\right). \tag{8}$$

Therefore, the corresponding standard deviations of the normalized components of the effective elastic modulus for a d-dimensional random polycrystal read:

$$\sigma_{\hat{C}_{IJ}^{\mathrm{eff}}}(d) \approx \frac{\alpha'_{IJ}(d)}{\sqrt{N_g}} \sqrt{\frac{\overline{D^{2d}}}{\overline{D^d}^2}} = \frac{\alpha'_{IJ}(d)}{\sqrt{N_g}} \left(1 + \delta_D^2\right)^{\frac{d^2}{2}}, \tag{9}$$

where $\alpha'_{IJ}(2) = \sqrt{1/32}$ regardless of IJ, and $\alpha'_{IJ}(3) = (\sqrt{16/525}, \sqrt{9/525})$ for $IJ = 11$ and $IJ = 12$, respectively. Note that the right-hand side of

Eq. (9) is for the particular case where the grain equivalent diameters follow a lognormal distribution. For this case, D^n ($n \in \mathbb{N}$) also follows a lognormal distribution whose mean is $\overline{D^n} = \overline{D}^n(1+\delta_D^2)^{\frac{n(n-1)}{2}}$. It is worth pointing out that for 3D polycrystals $\sigma_{\hat{C}_{11}^{\text{eff}}} = \sigma_{\hat{C}_{22}^{\text{eff}}} = \sigma_{\hat{C}_{33}^{\text{eff}}}$, $\sigma_{\hat{C}_{12}^{\text{eff}}} = \sigma_{\hat{C}_{13}^{\text{eff}}} = \sigma_{\hat{C}_{23}^{\text{eff}}} = \sigma_{\hat{C}_{44}^{\text{eff}}} = \sigma_{\hat{C}_{55}^{\text{eff}}} = \sigma_{\hat{C}_{66}^{\text{eff}}}$, and $\sigma_{\hat{C}_{11}^{\text{eff}}}/\sigma_{\hat{C}_{12}^{\text{eff}}} \approx 4/3$ regardless the grain size distribution. However, the standard deviations of all the components of C^{eff} are equal for a 2D random polycrystal. Comparing Eq. (9) with Eq. (4), one can get the theoretical values $\alpha_{IJ} = \alpha'_{IJ}(1+\delta_D^2)$ and $\beta_{IJ} = -0.5$ for the case where D follows a lognormal distribution. As such, even though the random variables C_{IJ}^{eff} and thus their variances depend on the local elastic moduli, their normalized counterparts $\hat{C}_{IJ}^{\text{eff}}$, when $\epsilon = 0$, have variances that are independent of the material properties.

We now proceed to generate different sets of synthetic polycrystals with varying widths for the grain size distributions, characterized by $\delta_D \approx \{0.11, 0.40\}$. For the sake of brevity, only 3D samples are generated. The corresponding values obtained from the numerical samples are provided in Table 5. Note that for each set, 200 cubic realizations ($1000\,\mu\text{m} \times 1000\,\mu\text{m} \times 1000\,\mu\text{m}$) are generated.

Fig. 7 illustrates the convergence of $\sigma_{\hat{C}_{11}^{\text{eff}}}$ in terms of the number of realizations N_{real}. As expected, more realizations are required by increasing the dispersion level of the grain size δ_D in order to get statistical convergence of $\sigma_{\hat{C}_{IJ}^{\text{eff}}}$. This figure reveals a close agreement between the analytical estimations (Eq. (9)) and the ones obtained numerically using 200 realizations for all the cases. The theoretical and numerical estimations for all the datasets are compared in Fig. 8, from which it can be observed that the results ob-

Table 5: Polycrystal sample sets with grain size distributions and their corresponding N_g and δ_D.

Set	N_g	δ_D	**Set**	N_g	δ_D
PSD11-1	586	0.106	**PSD40-1**	387	0.393
PSD11-2	1172	0.106	**PSD40-2**	772	0.394
PSD11-3	5844	0.106	**PSD40-3**	3857	0.393
PSD11-4	11707	0.107	**PSD40-4**	7680	0.396
PSD11-5	17517	0.107	**PSD40-5**	11562	0.394
PSD11-6	23478	0.107	**PSD40-6**	15497	0.395
PSD11-7	29182	0.107	**PSD40-7**	19262	0.394
PSD11-8	35151	0.107	**PSD40-8**	23202	0.395

tained from the analytical formula align closely with the numerical results.

3.1.3. Extension to bimodal grain size distributions

This section extends our previous analytical formulations to the case of polycrystals with bimodal grain size distributions. The polycrystals comprise two subgroups of grains: small grains (sg) following one size distribution and large grains (lg) following another. Thus, the equivalent grain diameter random variable is distributed as $D \sim \frac{N_{\text{sg}}}{N_g} D_{\text{sg}} + \frac{N_{\text{lg}}}{N_g} D_{\text{lg}}$, where N_{sg} and $N_{\text{lg}} = N_g - N_{\text{sg}}$ are the numbers of small and large grains inside the polycrystalline sample and D_{sg} and D_{lg} denote the corresponding equivalent diameters random variables, respectively. In this case, Eq. (5) can be

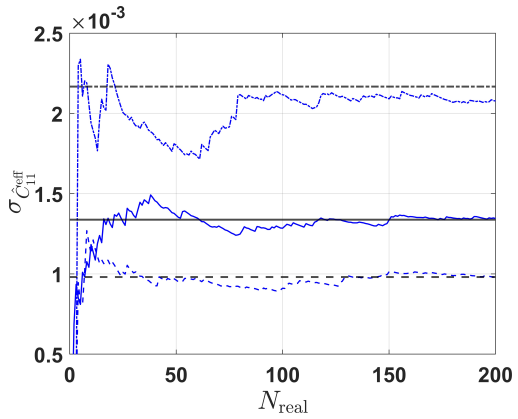

Figure 7: (Color online) Theoretical results (black lines) and numerical results (blue lines) of $\sigma_{\hat{C}_{11}^{\text{eff}}}$ for the case **PSD11-8** (dashed lines), **PSD26-8** (solid lines), and **PSD40-8** (dash-dotted lines).

rewritten as:

$$\hat{C}_{IJ}^{\text{eff}} = \hat{C}_{IJ}^{\text{eff,iso}}(h) + \phi_1 \frac{\sum_{m=1}^{N_{\text{sg}}} f_{IJ_m} V_m}{\sum_{m=1}^{N_{\text{sg}}} V_m} + \phi_2 \frac{\sum_{n=1}^{N_{\text{lg}}} f_{IJ_n} V_n}{\sum_{n=1}^{N_{\text{lg}}} V_n}, \tag{10}$$

where ϕ_1 and $\phi_2 = 1 - \phi_1$ are the volume fractions of the small and large grains, respectively. Subsequently, Eq. (9) can be extended as:

$$\begin{aligned} \sigma_{\hat{C}_{IJ}^{\text{eff}}} &\approx \alpha'_{IJ}(d) \sqrt{\frac{\phi_1^2}{N_{\text{sg}}} \frac{\overline{D_{\text{sg}}^{2d}}}{\overline{D_{\text{sg}}^{d}}^2} + \frac{\phi_2^2}{N_{\text{lg}}} \frac{\overline{D_{\text{lg}}^{2d}}}{\overline{D_{\text{lg}}^{d}}^2}} \\ &= \alpha'_{IJ}(d) \sqrt{\frac{\phi_1^2}{N_{\text{sg}}} \left(1 + \delta_{D_{\text{sg}}}^2\right)^{d^2} + \frac{\phi_2^2}{N_{\text{lg}}} \left(1 + \delta_{D_{\text{lg}}}^2\right)^{d^2}}, \end{aligned} \tag{11}$$

where $\alpha'_{IJ}(d)$ takes the same values as mentioned earlier.

The 3D polycrystal samples with bimodal grain size distributions were subsequently generated using NEPER [40]. It is worth mentioning that generating samples with bimodal grain size distributions requires significantly

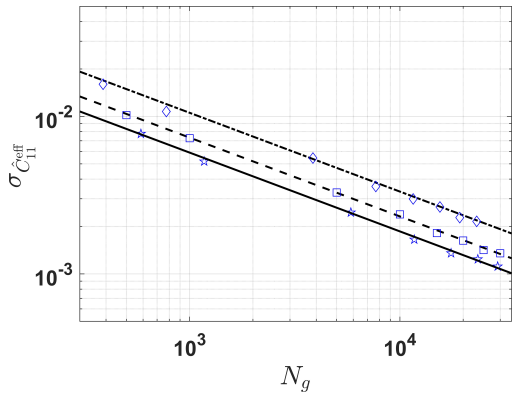

Figure 8: (Color online) Numerical estimation of $\sigma_{\hat{C}_{11}^{\text{eff}}}$ for the 3D polycrystal sample sets **PSD11** ($\delta_D \approx 0.11$, pentagram marker), **PSD26** ($\delta_D \approx 0.26$, square marker), and **PSD40** ($\delta_D \approx 0.40$, diamond marker), compared with the corresponding theoretical estimations in black solid, black dashed, and black dashed-dotted lines, respectively.

more CPU time than those with unimodal distributions. Therefore, we only consider two different sample sets for our numerical investigations, each containing 200 distinct realizations. Detailed morphological information is reported in Table 6. Fig. 9(a) shows one realization of the polycrystal sample set **PSB-2**, where the green and red colors are used to distinguish small and large grains, respectively. The PDF of the equivalent diameter D is depicted in Fig. 9(b) where a bimodal distribution can be observed.

Table 6: Polycrystal sample sets with bimodal grain size distributions and their corresponding morphological information.

Set	N_{lg}	$\bar{D}_{\text{lg}}$ [μm]	$\delta_{D_{\text{lg}}}$	N_{sg}	$\bar{D}_{\text{sg}}$ [μm]	$\delta_{D_{\text{sg}}}$
PSB-1	753	225.7	0.11	4365	72.1	0.30
PSB-2	5584	223.6	0.14	13312	103.1	0.16

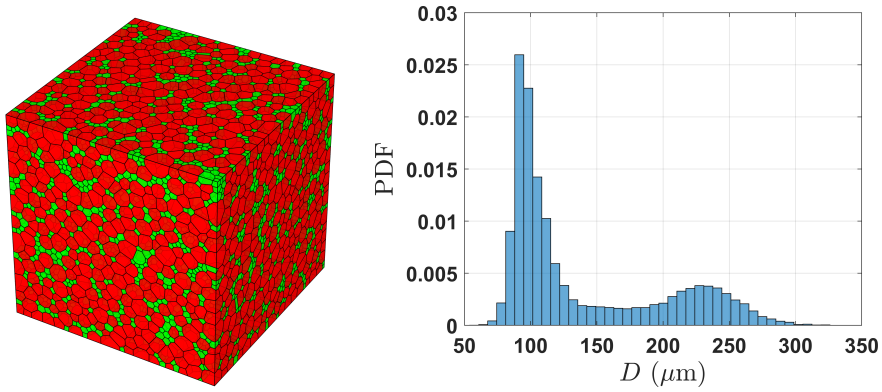

(a) (b)

Figure 9: (Color online) (a) A realization of the polycrystal sample set **PSB-2**, where smaller (resp. larger) grains are depicted in green (resp. red), and (b) the PDF of its grain equivalent diameter D.

Fig. 10 presents the numerical (blue) and analytical (black) estimations of $\sigma_{\hat{C}_{11}^{\text{eff}}}$ in terms of the number of realizations. It can be observed that the numerical results slightly underestimate the analytical results for both cases. This discrepancy may arise from an inadequate representation of the larger grains ($N_{\text{lg}} = 753$) and an insufficient number of realizations, particularly in the case of **PSB-1**. Although 200 realizations were employed to estimate $\sigma_{\hat{C}_{11}^{\text{eff}}}$, as shown in Fig. 10, it is evident that the estimated value fails to converge, yet approaches the analytical target more closely by increasing the number of realizations. By incorporating a sufficient number of small and large grains in the polycrystal models and increasing the number of realizations, we expect the numerical estimations to converge to the analytical results.

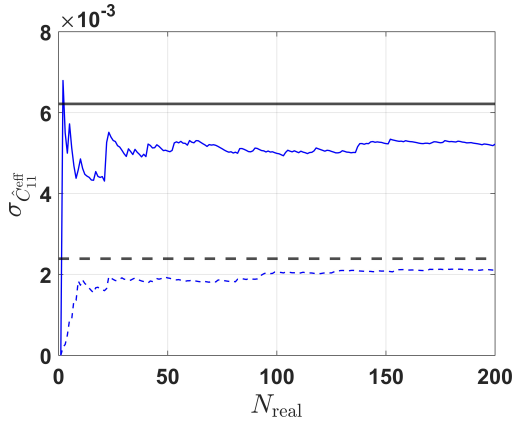

Figure 10: (Color online) Numerical estimation of $\sigma_{\hat{C}_{11}^{\text{eff}}}$ for the polycrystal sample set **PSB-1** (resp. **PSB-2**) in blue solid line (resp. blue dashed line), compared with the corresponding theoretical estimations in black solid (resp. black dashed line).

3.1.4. Influence of random local elasticity tensor

In this section, we aim to extend the aforementioned analytical formulas to the case where different polycrystalline samples have discrepancies in the elastic constants of their grains expressed in the crystallite local axes, i.e., $C^{(\text{cr})}$. To this end, realizations of the random SEC are generated using Eqs. (2) such that each value of the matrix $C^{(\text{cr})}$ is assigned to all the grains of each sample. The dispersion level ϵ characterizes the fluctuation level of the component C_{44} between different samples of each set. For the particular case of alpha iron (α-Fe) with $\epsilon = 0$ (reference case) and $\epsilon = 0.02$ (case based on the experimental values), the distributions of the component C_{44} estimated using 200 realizations are depicted in Fig. 11, where the vertical line corresponds to the deterministic case $\epsilon = 0$, or equivalently $C_{IJ} \sim \delta(x - \bar{C}_{IJ})$, in which δ is the Dirac delta distribution.

We first analytically study the impact of the dispersion level ϵ on the

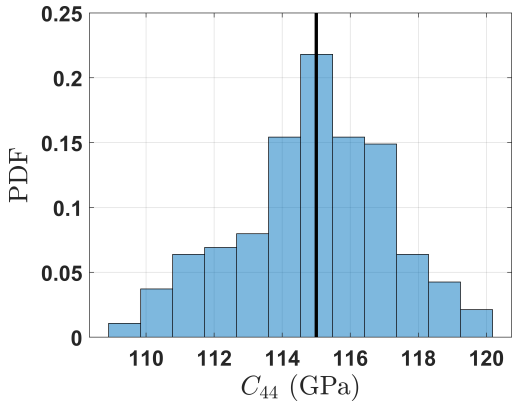

Figure 11: (Color online) Distributions of C_{44} estimated using 200 realizations of the set **PSD26-4** composed of alpha iron (α-Fe) grains, for different dispersion levels $\epsilon = 0$ (black solid line), and $\epsilon = 0.02$ (histogram).

second-order statistics of C^{eff}. Here, the Euler angles are considered uncorrelated (case RF_{unc} in Table 4). If $\epsilon \neq 0$, contrary to the previous cases, both isotropic and anisotropic parts will contribute to the values of $\sigma_{\hat{C}_{IJ}^{\text{eff}}}$. However, ϵ is influential only on the contribution of the isotropic part. Since these two parts are uncorrelated, one can write:

$$\sigma_{\hat{C}_{IJ}^{\text{eff}}} = \sqrt{\text{Var}\left(\hat{C}_{IJ}^{\text{eff,iso}}\right) + \text{Var}\left(\hat{C}_{IJ}^{\text{eff,ani}}\right)}. \tag{12}$$

Recall that the normalization is defined as $\hat{C}_{IJ}^{\text{eff,iso}}(h,\epsilon) = C_{IJ}^{\text{eff,iso}}(h)/\nu_{\text{sc}}(h,\epsilon)$ for the general SC-based averaging. The particular case of Voigt averaging occurs when $h = 0$. The second term at the RHS of this equation is independent of the material properties and has been derived in Eq. (9). On the contrary, the first term depends on the average elastic moduli $(\bar{C}_{11}, \bar{C}_{12}, \bar{C}_{44})$ and the dispersion level ϵ. The former is independent of N_g and the grain size statistics. Similar to our previous calculations, we use Eq. (8) to approximately calculate the variance of the isotropic part. The analytical expressions

for the SC homogenization are complicated because of the highly nonlinear dependence on the local elastic moduli random variables. In the sequel, we only consider the Voigt averaging ($h = 0$). In this case, one can show that the variance of the components of the isotropic part could be decomposed as $\mathrm{Var}(\hat{C}_{IJ}^{\mathrm{eff,iso}}) \approx \epsilon^2 \mathcal{G}_{IJ}^{(1)} \mathcal{G}_{IJ}^{(2)}$, where $\mathcal{G}_{IJ}^{(m)}$, ($m \in \{1, 2\}$) are given in Appendix B, Eqs. (B.1). Subsequently, a numerical investigation based on the polycrystal sample sets **PSD26** (Table 1) composed of different cubic materials (Table 2) has been performed. Fig. 12 illustrates the comparison between the numerical and analytical values of $\sigma_{\hat{C}_{11}^{\mathrm{eff}}}$ ($d = 3$). The agreement between them is observed, especially for polycrystals having a larger number of grains. Moreover, incorporating fluctuations of the local elastic properties into the model leads to an increase in the values of $\sigma_{\hat{C}_{IJ}^{\mathrm{eff}}}$, compared to the reference case ($\epsilon = 0$). It is worth noting that since $\mathrm{Var}(\hat{C}_{11}^{\mathrm{eff,iso}})$ depends on the material properties, it is no longer possible to obtain a master curve. Fig. 12 also shows that the contribution of the isotropic part that is independent of N_g is dominant (compared to that of the anisotropic part) such that the dependence of $\sigma_{\hat{C}_{11}^{\mathrm{eff}}}$ to N_g is negligible. The values of $\sigma_{\hat{C}_{IJ}^{\mathrm{eff}}}$ for materials with lower average anisotropy levels, e.g., aluminum (Al), are significantly larger than the ones with higher average anisotropy degrees, e.g., lithium (Li). To further investigate that, we summarize in Table 7 and for different materials, the contributions of the isotropic part to the variance, described by the functions $\mathcal{G}_{IJ}^{(m)}$ with $m \in \{1, 2\}$ and $IJ \in \{11, 12, 66\}$. The values reveal that by increasing the mean anisotropy level, both contributions are decreasing such that the values of $\sigma_{\hat{C}_{11}^{\mathrm{eff}}}$ decrease as well.

In conclusion, our study shows the substantial influence of small fluctu-

ations in local stiffness tensors on the statistical characteristics of effective elastic moduli. One can predict that these variations not only influence the overall elastic properties but also can have a significant impact on the plastic behaviors of polycrystalline materials by introducing higher variability in critical material properties, e.g., yield strain, yield stress, ultimate tensile strength, and fracture toughness. Furthermore, in the context of two-phase polycrystals, the local stiffness tensor may exhibit larger fluctuations, thereby increasing the discrepancy in the mechanical response observed across various realizations of polycrystal samples. In future numerical studies, considering this stochastic local stiffness tensor is essential for the uncertainty quantification and the comprehensive assessment of material structural integrity, ductility, and safety margins.

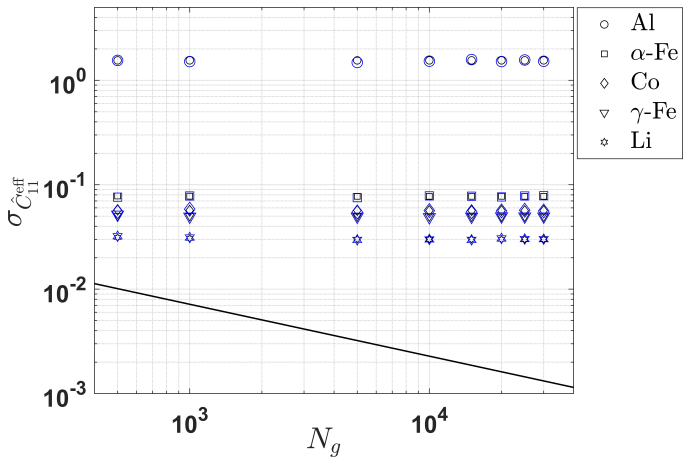

Figure 12: (Color online) Comparison of numerical (big blue markers) and analytical results (small black markers) of $\sigma_{\hat{C}_{11}^{\text{eff}}}$ for five cubic materials when $\epsilon = 0.02$. The reference case $\epsilon = 0$ is shown in black solid line.

Table 7: Values of the functions $\mathcal{G}_{IJ}^{(m)}$ ($m \in \{1,2\}$, $IJ \in \{11,12,66\}$) for the materials listed in Table 2.

Material	$\hat{A}$	$\mathcal{G}_{11}^{(1)}$	$\mathcal{G}_{11}^{(2)}$	$\mathcal{G}_{12}^{(1)}$	$\mathcal{G}_{12}^{(2)}$	$\mathcal{G}_{66}^{(1)}$	$\mathcal{G}_{66}^{(2)}$
Al	0.23	125.19	48.14	34.21	58.29	7.13	47.08
α-Fe	1.40	7.42	2.02	1.02	7.88	0.74	1.28
Co	2.12	5.72	1.40	0.85	6.41	0.54	0.56
γ-Fe	3.81	5.12	1.20	1.00	5.18	0.40	0.17
Li	8.14	3.18	0.71	0.44	4.65	0.32	0.04

3.2. Statistical properties of the phase velocities

In this section, the phase velocities are calculated by solving the Christoffel equation (Eq. (3)), and their statistical behaviors are subsequently examined. In the previous sections, the significance of the spatially correlated crystallographic orientations, randomness in the local elastic matrix, and the width of the grain size PDF on the standard deviations of different components of the effective matrix C^{eff} have been highlighted. Given the dependence of the phase velocities on the background elastic moduli C^{eff}, their variability will be explored in this section.

Let the propagation direction be $\hat{\mathbf{k}} = [1\ 0\ 0]^\top$, the phase velocities of the modes $i \in \{\text{qP}, \text{qS}_1, \text{qS}_2\}$ can be obtained via $\rho \mathtt{V}_i^2 = C_{IJ}^{\text{eff}}$ where $IJ \in \{11, 66, 55\}$, respectively. Recall that based on our analytical formulas we have $\sigma_{\hat{C}_{44}^{\text{eff}}} = \sigma_{\hat{C}_{55}^{\text{eff}}} = \sigma_{\hat{C}_{66}^{\text{eff}}}$. As such, analytically, no difference will be made between qS_1 and qS_2 modes. We further define the normalized phase velocity of the mode i as $\hat{\mathtt{V}}_i = \rho \mathtt{V}_i^2 / \nu_{\text{sc}}(h)$. In the case of a random polycrystal having uncorrelated Euler angles, using Eq. (9), one can calculate the variance of

$\hat{\mathtt{V}}_i$ as $\mathrm{Var}(\hat{\mathtt{V}}_i) = \mathrm{Var}(\hat{C}_{IJ}^{\mathrm{eff}})$. For the particular case where $\epsilon = 0$, we can further use the following Taylor expansion-based approximation to link the variances of the squared phase velocities to those of the phase velocities, i.e., $\mathrm{Var}(\hat{\mathtt{V}}_i) \approx 2\rho^2 \mathrm{Var}(\mathtt{V}_i)\bar{\mathtt{V}}_i/\nu_{\mathrm{sc}}^2$ such that by introducing in Eq. (9) for $d = 3$ we get the following estimation for the standard deviation of the phase velocities:

$$\sigma_{\mathtt{V}_i} \approx \frac{\alpha'_{IJ}(3)|\nu_{\mathrm{sc}}|}{\rho\sqrt{2N_g}\bar{\mathtt{V}}_i}\sqrt{\frac{\overline{D^6}}{\overline{D^3}^2}} = \frac{\alpha'_{IJ}(3)|\nu_{\mathrm{sc}}|}{\rho\sqrt{2N_g}\bar{\mathtt{V}}_i}\left(1+\delta_D^2\right)^{4.5}. \tag{13}$$

Fig. 13 illustrates, for all previously defined 3D samples, the influence of δ_D on the standard deviation of normalized phase velocities, i.e., $\sigma_{\hat{\mathtt{V}}_i}$ when the orientations are uncorrelated and $\epsilon = 0$. Similar to the effective elastic moduli, increasing the CV of the grain diameters leads to higher variations in the phase velocities for both P and S waves. Additionally, when δ_D takes on a relatively small value, say $\delta_D \approx 0.11$, the difference between the values of $\sigma_{\hat{\mathtt{V}}_{\mathrm{S}_1}}$ and $\sigma_{\hat{\mathtt{V}}_{\mathrm{S}_2}}$ vanishes. However, as δ_D increases, a slight deviation between the standard deviations of the S modes emerges, implying that the background properties of the polycrystals are more anisotropic.

Based on Eq. (13), the standard deviation of P (or S) wave phase velocities can be expressed as a function of several key parameters, including the number of grains N_g, the CV of grain size distribution δ_D, the density ρ, and the local elastic properties. This equation thus allows us to identify the polycrystal morphology through phase velocity measurements. The NDE techniques (e.g., based on the measurements of scattering-induced attenuation) can be employed to measure the mean and standard deviation (and thus δ_D) of the grain size random variable [34, 35]. Given the known volume of the sample, a rough estimation for the number of grains N_g can be ob-

tained via $N_g \approx V_{tot}/\bar{V} = V_{tot}/\left(\frac{\pi}{6}\bar{D}^3(1+\delta_D^2)^3\right)$, where V_{tot} denotes the total volume of the sample. According to the known estimations for δ_D, N_g, and the mechanical properties of the material, the statistical properties of the phase velocities can be calculated using Eq. (13). At this stage, by assuming the statistical homogeneity of the phase velocities, one can estimate their standard deviations based on measurements at different points of the sample. By comparing the latter with the analytical standard deviations (based on Eq. (13)), regions exhibiting significantly distinct morphological properties compared to the entire sample can be identified. Specifically, in casting alloys like steel, where grain sizes can vary significantly across different regions of the samples [58] due to the manufacturing process, our measurements, which rely on the assessment of phase velocity variations, serve as a valuable tool for pinpointing areas with larger discrepancies in grain size distributions. Besides, this approach also allows us to estimate the number of grains N_g, provided that the experimental measures of the phase velocities are available and that the values of δ_D and the mechanical properties are known. Finally, this approach also enables non-destructive identification of the CV for grain sizes δ_D, using the rough estimator introduced for N_g and experimental measurements of the phase velocities. It should be noted that contrary to this approach, using the EBSD technique entails sample destruction and provides localized measurements that may not adequately capture the whole properties of the samples.

Besides, for the case where $\epsilon \neq 0$ can be similarly dealt with using Eq. (12) along with Eqs. (9) and (B.1). Fig. 14 presents the impact of ϵ on the $\sigma_{\hat{\mathbb{V}}_{\mathrm{P}}}$ and $\sigma_{\hat{\mathbb{V}}_{\mathrm{S}_1}}$. It is worth recalling the difference between $\sigma_{\hat{\mathbb{V}}_{\mathrm{S}_1}}$ and $\sigma_{\hat{\mathbb{V}}_{\mathrm{S}_2}}$ is negligible. As

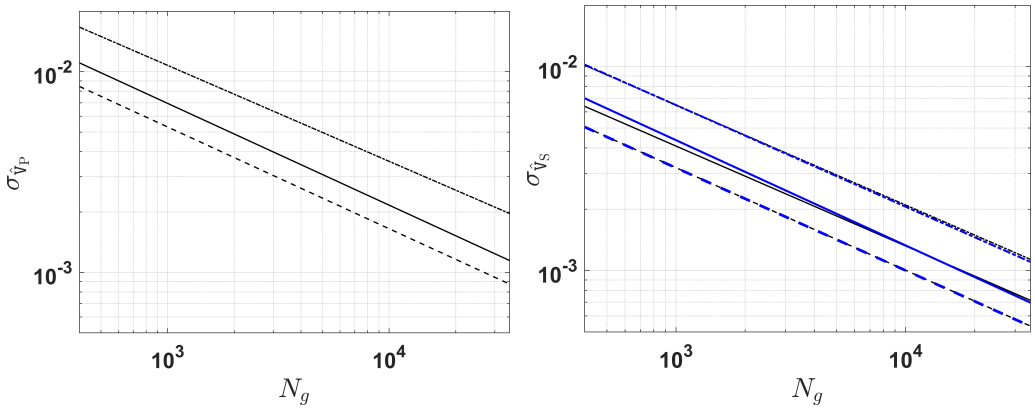

Figure 13: (Color online) Estimation of (a) $\sigma_{\hat{\mathbb{V}}_P}$, and (b) $\sigma_{\hat{\mathbb{V}}_{S_1}}$ (black thin lines), $\sigma_{\hat{\mathbb{V}}_{S_2}}$ (blue thick lines) for different materials in polycrystal sample sets **PSD11** (dashed lines), **PSD26** (solid lines), and **PSD40** (dashed-dotted lines) when $\epsilon = 0$.

expected, a universal line is attained for all materials when $\epsilon = 0$. Moreover, for $\epsilon = 0.02$, the variabilities of the P and S wave velocities experience a significant increase. For the polycrystals of aluminum (Al) having 30000 grains and $\epsilon = 0.02$, $\sigma_{\hat{\mathbb{V}}_P}$ and $\sigma_{\hat{\mathbb{V}}_{S_1}}$ are around 2818 and 1005 times (three orders of magnitude) larger than the case where $\epsilon = 0$, respectively. As such, considering the dispersion level ϵ of the local stiffness tensor is necessary when using ultrasonic phase velocity measurements to evaluate the microstructural information of polycrystals, especially those with low anisotropy levels.

4. Conclusions

This study presents an investigation into the statistical properties of the effective elastic moduli and phase velocities based on synthetic polycrystals

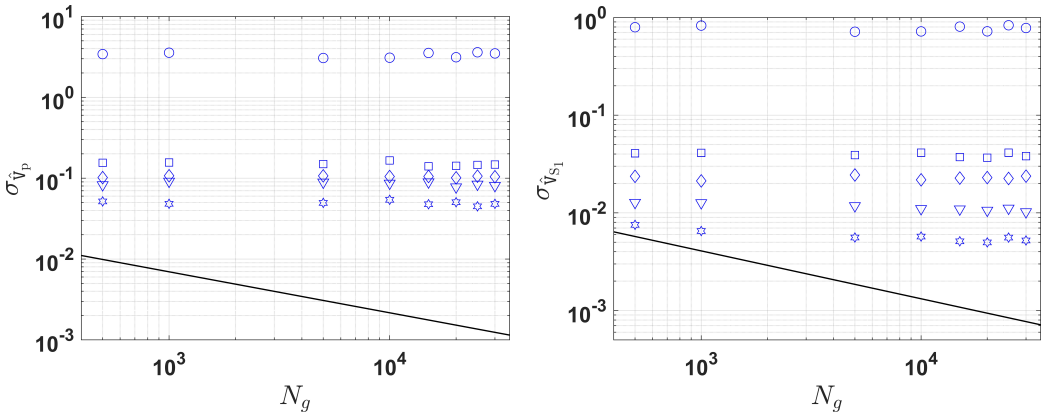

Figure 14: (Color online) Estimation of (a) $\sigma_{\hat{\mathbb{V}}_{\mathrm{P}}}$, and (b) $\sigma_{\hat{\mathbb{V}}_{\mathrm{S}_1}}$ for different materials in sample set **PSD26** when $\epsilon = 0.02$ (blue markers), and $\epsilon = 0$ (black solid line).

composed of cubic materials. The influence of correlated crystallographic orientations with varying correlation functions and correlation lengths has been examined. The statistical behavior of homogenized elastic properties remains almost unchanged compared to independent (uncorrelated) orientations when the Euler angles have a relatively short correlation length compared to the typical grain size. Analytical formulas have been derived to estimate the standard deviation of the effective elastic moduli for two- and three-dimensional polycrystals having unimodal or bimodal grain size distributions. The former showed excellent agreement with our numerical results. Furthermore, the introduction of a relatively small fluctuation in the local stiffness tensor between different realizations has led to a significant increase in the variability of the homogenized elastic properties and phase velocities, particularly for cubic materials with lower anisotropy levels. The impact of

the fluctuation in the local stiffness tensor, as well as that of the grain size distribution, on the statistical properties of ultrasonic phase velocities have been investigated. Particularly, we have provided an explicit equation linking the second-order statistics of phase velocities with some critical morphological parameters in polycrystals, i.e., the number of grains N_g and, notably, the width of the grain size distribution δ_D. Future experiments can refer to Eq. (13) to utilize second-order phase velocity statistics to determine either N_g or δ_D, as well as to assess the grain morphology uniformity across different regions in polycrystalline samples. Our ongoing research includes extending these results to cases involving elliptical grain shapes and two-phase polycrystalline materials.

Declaration of Competing Interest

The authors declare that they have no known competing financial interests or personal relationships that could have appeared to influence the work reported in this paper.

Acknowledgments

This research was funded by Ministère de l'Enseignement Supérieur et de la Recherch et de l'Innovation (MESRI), France. A CC-BY public copyright license has been applied by the authors to the present document and will be applied to all subsequent versions up to the Author Accepted Manuscript arising from this submission, in accordance with the grant's open access conditions. Additionally, we gratefully acknowledge the support of the Centre de Calcul Intensif des Pays de la Loire (CCIPL), France.

Appendix A.

We use the experimental results of elastic constants of alpha iron (α-Fe) monocrystals summarized by Cantara *et al.* [15] (see Table A1 and references therein).

Table A.1: The SEC of alpha iron (α-Fe) monocrystals, determined at room temperature ($\sim$300 K) and atmospheric pressure using either the ultrasonic pulse-echo technique or resonant ultrasonic spectroscopy [15].

	c_{11} [GPa]	c_{12} [GPa]	c_{44} [GPa]
1	236.88	140.63	116.01
2	241.50	146.63	111.73
3	228.09	133.48	110.86
4	209.36	113.66	111.36
5	242.00	146.50	112.00
6	237.00	141.00	116.00
7	233.10	135.44	117.83
8	228.00	132.00	116.50
9	223.00	127.00	115.00
10	231.40	134.70	116.40
11	230.10	134.60	116.60
12	226.00	140.00	116.00
13	232.20	135.60	117.00
14	231.50	135.00	116.00
15	230.37	134.07	115.87
$\bar{C}_{IJ}$	230.70	135.35	115.01
$\sigma_{C_{IJ}}$	7.94	7.98	2.29
$\delta_{C_{IJ}}$	0.03	0.06	0.02

Appendix B.

The explicit formulas for $\mathcal{G}_{IJ}^{(m)}$, $(m \in \{1,2\})$ write:

$$
\begin{aligned}
\mathcal{G}_{IJ}^{(1)} &= \left(\bar{C}_{IJ}^{\text{iso}}/(k_3 s_3 - k_2 s_2)\right)^2, \\
\mathcal{G}_{11}^{(2)} &= \frac{\frac{k_1 s_1^2}{\epsilon^2} + \frac{k_3 s_3^2}{\epsilon^2} + 9k_2^2 s_2^2}{(k_1 s_1 - k_3 s_3 + 3k_2 s_2)^2} \\
&+ \frac{2\left(\frac{k_3 s_3^2}{\epsilon^2} + 3k_2^2 s_2^2\right)}{(k_1 s_1 - k_3 s_3 + 3k_2 s_2)(k_3 s_3 - k_2 s_2)} + \frac{\frac{k_3 s_3^2}{\epsilon^2} + k_2^2 s_2^2}{(k_3 s_3 - k_2 s_2)^2}, \\
\mathcal{G}_{12}^{(2)} &= \frac{k_1 s_1^2 + k_3 s_3^2}{\epsilon^2 (k_1 s_1 - k_3 s_3)^2} \\
&+ \frac{2k_3 s_3^2}{\epsilon^2 (k_1 s_1 - k_3 s_3)(k_3 s_3 - k_2 s_2)} + \frac{\frac{k_3 s_3^2}{\epsilon^2} + k_2^2 s_2^2}{(k_3 s_3 - k_2 s_2)^2}, \\
\mathcal{G}_{44}^{(2)} &= 1 + \frac{k_2 s_2}{k_3 s_3 - k_2 s_2} + \frac{\frac{k_3 s_3^2}{\epsilon^2} + k_2^2 s_2^2}{(k_3 s_3 - k_2 s_2)^2},
\end{aligned}
\tag{B.1}
$$

in which k_n and s_n $(n \in \{1,2,3\})$ are the shape and scale parameters, respectively, defined in Eqs. (2).

References

[1] W. Voigt, Theoretische studien über die elasticitätsverhältnisse der krystalle ("Theoretical studies on the elasticity relationships of crystals"), Abh. Ges. Wiss. Göttingen 9 (1887) 3–51.

[2] A. Reuß, Berechnung der fließgrenze von mischkristallen auf grund der plastizitätsbedingung für einkristalle. ("Estimation of the yield strength of polycrystals based on the plastic behavior of single crystals"), J. Appl. Math. Mech. 9 (1929) 49–58.

[3] E. Kröner, Berechnung der elastischen konstanten des vielkristalls aus den konstanten des einkristalls ("Calculation of the elastic constants of polycrystals from the single-crystal constants"), Z. Phys. 151 (1958) 504–518.

[4] H. Seiner, L. Bodnárová, P. Sedlák, M. Janeček, O. Srba, R. Král, M. Landa, Application of ultrasonic methods to determine elastic anisotropy of polycrystalline copper processed by equal-channel angular pressing, Acta Mater. 58 (2010) 235–247.

[5] G. Abrosimova, N. Afonikova, Y. Estrin, N. Kobelev, E. Kolyvanov, Orientation dependence of elastic properties and internal stresses in sub-microcrystalline copper produced by equal channel angular pressing, Acta Mater. 58 (2010) 6656–6664.

[6] G. C. Johnson, Variations in the second-and third-order elastic constants in polycrystalline aggregates, J. Appl. Phys. 59 (1986) 4057–4061.

[7] T. Kanit, S. Forest, I. Galliet, V. Mounoury, D. Jeulin, Determination of the size of the representative volume element for random composites: statistical and numerical approach, Int. J. Solids Struct. 40 (2003) 3647–3679.

[8] T. Böhlke, K. Jöchen, O. Kraft, D. Löhe, V. Schulze, Elastic properties of polycrystalline microcomponents, Mech. Mater. 42 (2010) 11–23.

[9] M. Norouzian, J. A. Turner, Ultrasonic wave propagation predictions for polycrystalline materials using three-dimensional synthetic microstruc-

tures: Phase velocity variations, J. Acoust. Soc. Am. 145 (2019) 2171–2180.

[10] S. M. Qidwai, D. M. Turner, S. R. Niezgoda, A. C. Lewis, A. B. Geltmacher, D. J. Rowenhorst, S. R. Kalidindi, Estimating the response of polycrystalline materials using sets of weighted statistical volume elements, Acta Mater. 60 (2012) 5284–5299.

[11] F. El Houdaigui, S. Forest, A. F. Gourgues, D. Jeulin, On the size of the representative volume element for isotropic elastic polycrystalline copper, in: IUTAM Symposium on Mechanical Behavior and Micro-Mechanics of Nanostructured Materials: Proceedings of the IUTAM Symposium held in Beijing, China, June 27–30, 2005, Springer, 2007, pp. 171–180.

[12] J. Kim, R. Golle, H. Hoffmann, Investigation of size effects of very thin aluminum and copper sheets using aero-bulge test, Mater. Sci. Eng. A. 527 (2010) 7220–7224.

[13] F. Chen, S. Chen, X. Dong, C. Li, X. Hong, X. Zhang, Size effects on tensile strength of aluminum–bronze alloy at room temperature, Mater. Des. 85 (2015) 778–784.

[14] P.-A. Dubos, E. Hug, S. Thibault, M. Ben Bettaieb, C. Keller, Size effects in thin face-centered cubic metals for different complex forming loadings, Metall. Mater. Trans. A. 44 (2013) 5478–5487.

[15] A. M. Cantara, M. Zecevic, A. Eghtesad, C. M. Poulin, M. Knezevic,

Predicting elastic anisotropy of dual-phase steels based on crystal mechanics and microstructure, Int. J. Mech. Sci. 151 (2019) 639–649.

[16] H. J. Bunge, Orientation Distributions, in: H. J. Bunge (Ed.), Texture Analysis in Materials Science, Butterworth-Heinemann, 1982, pp. 42–46.

[17] S. I. Wright, B. L. Adams, K. Kunze, Application of a new automatic lattice orientation measurement technique to polycrystalline aluminum, Mater. Sci. Eng. A. 160 (1993) 229–240.

[18] A. Noshadravan, R. Ghanem, J. Guilleminot, I. Atodaria, P. Peralta, Validation of a probabilistic model for mesoscale elasticity tensor of random polycrystals, Int. J. Uncertain. Quantif. 3 (2013).

[19] S. R. Arwade, M. Grigoriu, Probabilistic model for polycrystalline microstructures with application to intergranular fracture, J. Eng. Mech. 130 (2004) 997–1005.

[20] X. Gao, C. Przybyla, B. Adams, Methodology for recovering and analyzing two-point pair correlation functions in polycrystalline materials, Metall. Mater. Trans. A. 37 (2006) 2379–2387.

[21] B. Adams, P. Morris, T. Wang, K. Willden, S. Wright, Description of orientation coherence in polycrystalline materials, Acta Metall. 35 (1987) 2935–2946.

[22] L. Germain, N. Gey, M. Humbert, P. Vo, M. Jahazi, P. Bocher, Texture heterogeneities induced by subtransus processing of near α titanium alloys, Acta Mater. 56 (2008) 4298–4308.

[23] M. Grigoriu, Nearest neighbor probabilistic model for aluminum polycrystals, J. Eng. Mech. 136 (2010) 821–829.

[24] B. L. Adams, X. C. Gao, S. R. Kalidindi, Finite approximations to the second-order properties closure in single phase polycrystals, Acta Mater. 53 (2005) 3563–3577.

[25] N. Sheng, S. Khazaie, M. Chevreuil, S. Fréour, Statistical properties of effective elastic moduli of random cubic polycrystals, Mechanics & Industry 24 (2023) 33.

[26] F. Rhines, B. Patterson, Effect of the degree of prior cold work on the grain volume distribution and the rate of grain growth of recrystallized aluminum, Metall. Mater. Trans. A. 13 (1982) 985–993.

[27] Y. Liu, J. Zhou, X. Ling, Impact of grain size distribution on the multiscale mechanical behavior of nanocrystalline materials, Mater. Sci. Eng. A. 527 (2010) 1719–1729.

[28] S. Berbenni, V. Favier, M. Berveiller, Impact of the grain size distribution on the yield stress of heterogeneous materials, Int. J. Plast. 23 (2007) 114–142.

[29] J. J. Bucki, K. J. Kurzydłowski, Analysis of the effect of grain size uniformity on the flow stress of polycrystals: Part I: Studies of the relationship between the variance of grain volume and the variance of the grain area on polycrystal cross section, Mater. Charact. 29 (1992) 365–374.

[30] S. Berbenni, V. Favier, M. Berveiller, Micro–macro modelling of the effects of the grain size distribution on the plastic flow stress of heterogeneous materials, Comput. Mater. Sci. 39 (2007) 96–105.

[31] B. Flipon, C. Keller, L. G. de La Cruz, E. Hug, F. Barbe, Tensile properties of spark plasma sintered AISI 316L stainless steel with unimodal and bimodal grain size distributions, Mater. Sci. Eng. A. 729 (2018) 249–256.

[32] S. K. Vajpai, M. Ota, T. Watanabe, R. Maeda, T. Sekiguchi, T. Kusaka, K. Ameyama, The development of high performance Ti-6Al-4V alloy via a unique microstructural design with bimodal grain size distribution, Metall. Mater. Trans. A. 46 (2015) 903–914.

[33] A. Dobkowska, B. Adamczyk-Cieślak, D. Kuc, E. Hadasik, T. Płociński, E. Ura-Bińczyk, J. Mizera, Influence of bimodal grain size distribution on the corrosion resistance of Mg–4Li–3Al–1Zn (LAZ431), J. Mater. Res. Technol. 13 (2021) 346–358.

[34] A. P. Arguelles, J. A. Turner, Ultrasonic attenuation of polycrystalline materials with a distribution of grain sizes, J. Acoust. Soc. Am. 141 (2017) 4347–4353.

[35] X. Bai, Y. Zhao, J. Ma, Y. Liu, Q. Wang, Grain-size distribution effects on the attenuation of laser-generated ultrasound in α-titanium alloy, Materials. 12 (2018) 102.

[36] A. Renaud, B. Tie, A.-S. Mouronval, J.-H. Schmitt, Multi-parameter optimization of attenuation data for characterizing grain size distributions

and application to bimodal microstructures, Ultrasonics. 115 (2021) 106425.

[37] P. Palanichamy, A. Joseph, T. Jayakumar, B. Raj, Ultrasonic velocity measurements for estimation of grain size in austenitic stainless steel, NDT E Int. 28 (1995) 179–185.

[38] A. Moro, C. Farina, F. Rossi, Measurement of ultrasonic wave velocity in steel for various structures and degrees of cold-working, NDT E Int. 13 (1980) 169–175.

[39] P. Palanichamy, M. Vasudevan, T. Jayakumar, S. Venugopal, B. Raj, Ultrasonic velocity measurements for characterizing the annealing behaviour of cold worked austenitic stainless steel, NDT E Int. 33 (2000) 253–259.

[40] R. Quey, P. Dawson, F. Barbe, Large-scale 3D random polycrystals for the finite element method: Generation, meshing and remeshing, Comput. Methods Appl. Mech. Eng. 200 (2011) 1729–1745.

[41] J. Guilleminot, C. Soize, On the statistical dependence for the components of random elasticity tensors exhibiting material symmetry properties, J. Elast. 111 (2013) 109–130.

[42] R. Quey, L. Renversade, Optimal polyhedral description of 3d polycrystals: Method and application to statistical and synchrotron x-ray diffraction data, Comput. Methods Appl. Mech. Eng. 330 (2018) 308–333.

[43] R. G. Ghanem, P. D. Spanos, Stochastic Finite Elements: A Spectral Approach, Springer New York, 1991.

[44] M. Moakher, A. N. Norris, The closest elastic tensor of arbitrary symmetry to an elasticity tensor of lower symmetry, J. Elast. 85 (2006) 215–263.

[45] C. Soize, Random matrix theory for modeling uncertainties in computational mechanics, Comput. Methods Appl. Mech. Eng. 194 (2005) 1333–1366.

[46] A. V. Hershey, The Elasticity of an Isotropic Aggregate of Anisotropic Cubic Crystals, J. Appl. Mech. 21 (1954) 236–240.

[47] J. D. Eshelby, The determination of the elastic field of an ellipsoidal inclusion, and related problems, Proc. R. Soc. A: Math. Phys. Eng. Sci. 241 (1957) 376–396.

[48] H. M. Ledbetter, Monocrystal-polycrystal elastic constants of a stainless steel, Phys. Status Solidi A. 85 (1984) 89–96.

[49] V. A. Lubarda, New estimates of the third-order elastic constants for isotropic aggregates of cubic crystals, J. Mech. Phys. Solids. 45 (1997) 471–490.

[50] C. M. Kube, J. A. Turner, Ultrasonic attenuation in polycrystals using a self-consistent approach, Wave Motion. 57 (2015) 182–193.

[51] F. I. Fedorov, Theory of elastic waves in crystals, Springer Science & Business Media, 2013.

[52] C. M. Zener, Elasticity and Anelasticity of Metals, University of Chicago Press, Chicago, IL, 1948.

[53] A. Every, A. McCurdy, The elastic constants of crystals, in: D. F. Nelson (Ed.), Second and higher order elastic constants, Butterworth-Heinemann, 1992, pp. 1–634.

[54] C.-S. Man, R. Paroni, Y. Xiang, E. A. Kenik, On the geometric autocorrelation function of polycrystalline materials, J. Comput. Appl. Math. 190 (2006) 200–210.

[55] A. P. Argüelles, Von kármán spatial correlation function to describe wave propagation in polycrystalline media, J. Appl. Phys. 131 (2022).

[56] L. Klimeš, Correlation functions of random media, Pure Appl. Geophys. 159 (2002) 1811–1831.

[57] S. Khazaie, R. Cottereau, D. Clouteau, Influence of the spatial correlation structure of an elastic random medium on its scattering properties, J. Sound Vib. 370 (2016) 132–148.

[58] J. Reiter, C. Bernhard, H. Presslinger, Austenite grain size in the continuous casting process: Metallographic methods and evaluation, Materials Characterization 59 (2008) 737–746.